

Topoelectrical circuit realization of a Weyl semimetal heterojunction

S. M. Rafi-Ul-Islam ¹, Zhuo Bin Siu ¹ & Mansoor B. A. Jalil¹ 

Weyl semimetals (WSMs) are a recent addition to the family of topological materials, and the physical realization of heterojunctions between different types of WSMs is challenging. Here, we use electrical components to create topoelectrical (TE) circuits for modeling and studying the transmission across heterojunctions, consisting of a Type I WSM source to a drain in the Type II or intermediary Type III WSM phase. For transport from a Type I WSM source to a Type II WSM drain, valley-independent (dependent) energy flux transmission occurs when the tilt and transmission directions are perpendicular (parallel) to each other. Furthermore, “anti-Klein” tunneling occurs between a Type I source and Type III drain where the transmission is totally suppressed for certain valleys at normal incidence. Owing to their experimental accessibility, TE circuits offer an excellent testbed for transport phenomena in WSM-based heterostructures.

¹Department of Electrical and Computer Engineering, National University of Singapore, Singapore, Singapore. ✉email: elembaj@nus.edu.sg

Studies of the topological states of matter in various platforms, such as photonic^{1,2}, mechanical^{3,4}, and ultra-cold atom systems^{5,6}, and metamaterials^{7,8} and electrical networks^{9–11}, have emerged as one of the most exciting fields in contemporary condensed matter physics. Perhaps one of the most iconic features of such topological states is the existence of Weyl points in three-dimensional momentum space, at which electron and hole bands touch each other in the presence of either broken time reversal or crystal inversion symmetries. Materials with linear band dispersion in the vicinity of such exceptional points are generally classified as Weyl semimetals (WSM)^{12–14}. WSMs exhibit many novel characteristics such as negative magnetoresistance^{15,16}, exotic Fermi arc surface states^{14,17,18}, Klein tunneling^{19–21}, the quantum anomalous Hall effect^{22–24}, and the chiral magnetic effect^{25,26}. These outstanding and fascinating properties make WSMs ideal candidate materials for next-generation nanoelectronics and quantum computing^{27–30}.

A new class of WSM states with anisotropic dispersion that explicitly violates Lorentz invariance was recently proposed^{31,32}. The new WSM state, named the Type II WSM phase^{33,34}, exhibits many distinctive characteristics like anisotropic magnetoresistance³⁵ and anisotropic chiral anomaly^{36,37}. The existence of different types of WSMs based on their dispersion tilts opens yet another avenue for exploring their potential in device applications. However, the fabrication complexity of WSM material systems and lattice structural restrictions in tuning their properties and modulating their transport behavior present major challenges in the realization of device applications based on WSMs.

To overcome these limitations and explore new possibilities in WSMs, we consider a system known as a topoelectrical (TE) circuit³⁸ consisting of electrical components such as inductors and capacitors to not only model different WSM states, but also to study the transport phenomena between them. The term “topoelectrical circuit” was first introduced by Lee et al.¹¹. TE circuits offer the key advantage over condensed matter systems in that the system properties can be very easily tuned simply by changing the admittances of the circuit elements and the connections between them. The close correspondence between the TE network with the quantum tight binding (TB) model has motivated studies on the analogues of topological insulator states³⁹, quantum spin Hall states⁴⁰, topological corner states^{9,10}, and Chern insulator states⁴¹ based on electrical networks. Furthermore, the possible electrical detection (i.e., current, phase and impedance detection) of the Berry curvature⁴², topological edge states¹⁰, band structure⁴³, and the topological nodal states⁴⁰ in WSMs has been proposed in TE models. However, the transport between WSM phases has not yet been modeled in the corresponding TE circuits. Such transport studies in TE circuits would offer a unique platform into the topological behavior of WSM phases³⁸. For instance, the study of the effects of the tilt strength and direction on the transport properties in a WSM heterojunction may reveal many exotic features ranging from valley-selective transmission to large inter-valley scattering. In condensed matter systems, it may not be possible to fabricate clean interfaces nor manifest the Type I and Type II WSM phases simultaneously due to the different environmental conditions (e.g., temperature, strain, pressure, etc.) needed to exhibit these states in host material systems. In contrast, TE circuits can be implemented even on simple printed circuit boards, and offer much flexibility in tuning properties which allow for sharp and clean interfaces between different WSM phases.

In this work, we establish the analogy between a TE circuit and a quantum mechanical TB Hamiltonian for a condensed matter system. To validate the experimental feasibility of our TE circuit model, we give an explanation of the transformation of

an infinite lattice chain into a finite one in both one and multi-dimensional systems. We also explain in detail how to construct the TE analogues of Type I and Type II WSMs. Finally, we clarify the meaning of “transport” and “transmission” in the context of TE circuits. While transport carries the meaning of electron flux in condensed matter systems, we show that the analogous quantity in TE circuits is the flux of energy. We then calculate the analogue of the quantum mechanical transmission in a WSM heterojunction and reveal a key role played by the Dirac cone tilt direction in the transmission process for both types of WSMs. The transmitted energy flux across a TE analogue of a WSM heterojunction exhibits significant differences in the two cases where the transmission direction is parallel to the tilt direction, and where the transmission direction is perpendicular to the tilt direction. In the former case, the transmission shows a highly asymmetric valley profile where the energy flux transmission is significantly blocked in some valleys and only small transmission channels via inter-valley scattering are allowed. For the latter case, the transmission of energy flux shows identical profiles for all valleys. Thus, our analysis shows that TE circuits can be designed to provide an effective testbed for studying transport properties in WSM devices before they are realized in real material systems.

To investigate further, we consider the intermediate phase between Types I and II WSM, which we term as Type III WSM. The Type III WSM state shows a flat admittance band dispersion along its tilt direction. As a result, transmission across a heterojunction into a Type III WSM drain exhibits a unique transport behavior where total internal reflection occurs for some states at normal incidence to the interface, which we term as “anti-Klein” tunneling. This is in contrast to the maximum transmission at normal incidence for the case of transmission into a Type II WSM drain lead, which corresponds to the normal Klein tunneling. This pronounced difference in transport phenomena between the two different drain types is due to the fact that propagating states exist for only one of the two pseudospin branches in a Type III WSM, while in the case of Type II WSM, propagating modes exist for both of the pseudospin branches. The pseudospin mismatch between the incident source modes in some valleys and the drain modes results in the complete suppression of tunneling in the anti-Klein effect.

Results

Weyl semimetals in topoelectrical circuit. Appropriately constructed TE circuits can host the analogue of the WSM phase in which the C -bands disperse linearly with \vec{k} along all three spatial dimensions in the vicinity of the band-touching Weyl points. (Note that the C -bands of a TE circuit are the analogue of energy dispersion of a TB Hamiltonian, see the Methods section for details.) We consider the circuit depicted in Fig. 1 consisting of a regular array of repeating units along the x , y , and z directions. Each unit consists of an A sublattice site and B sublattice site, with each site comprising of a voltage node connected to the ground via the common grounding capacitance C and an “on-site potential” capacitance C_0 . Additionally, each A and B type node is grounded by a capacitor with capacitance $2C_{Bz}$ and $2C_{Az}$ respectively. The system has reflection symmetry along the z and y directions.

Denoting the A/B sublattice degree of freedom as the Pauli matrices σ_i , the TE Hamiltonian for the circuit in Fig. 1 reads

$$\begin{aligned}
 H(\vec{k}) = & ((C_{Az} + C_{Bz})\cos(k_z))\mathbf{I}_\sigma - (C_1(1 + \cos(k_x)) + C_y(2\cos(k_y)))\sigma_x \\
 & - C_1\sin(k_x)\sigma_y - (C_{Az} - C_{Bz})\cos(k_z)\sigma_z \\
 & + (2C_1 + 2C_y + 2C_{Az} + C_{Bz} + C_0)\mathbf{I}_\sigma.
 \end{aligned}
 \tag{1}$$

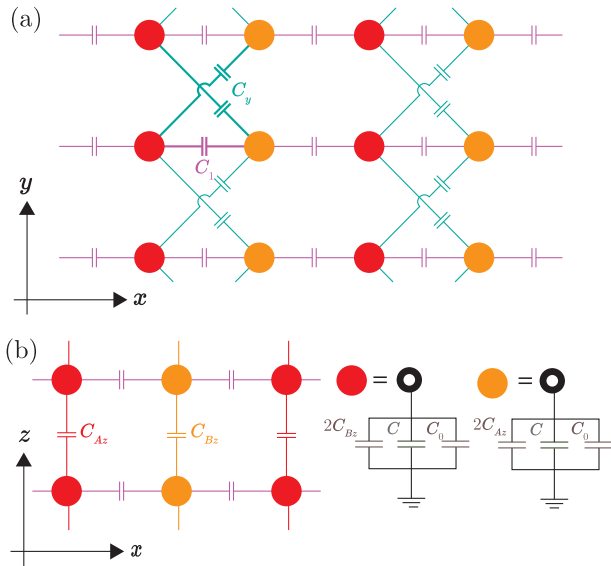


Fig. 1 Weyl semimetal (WSM) topoelectrical (TE) circuit. **a** Schematic of the xy plane of a TE circuit hosting the WSM state. **b** Schematic of the xz plane of the same TE circuit. The red and orange filled circles denote the A and B sublattice sites; each filled circle consists of a voltage node connected to the ground with an “on-site potential” capacitance C_0 and the common grounding capacitance C . Additionally, each A and B type node is grounded by a capacitor $2C_{Bz}$ and $2C_{Az}$ respectively.

The physical meaning of the Hamiltonian and the analogy between a TE circuit and a lattice Hamiltonian are explained in detail in the Methods section. For the convenience of the reader who would prefer not to read through the Methods section as this stage, the common grounding capacitance C is the experimentally tunable TE analogue of the Fermi energy, and the energy flux and node voltages are the TE analogues of the quantum particle current flux and wavefunction amplitude, respectively. The TE analogues of energy bands would thus be C -bands describing how the values of C and Bloch wavevectors k of the allowed voltage modes consistent with Kirchhoff’s laws are related to one another.

For convenience, we eliminate the terms in the last line of Eq. (1) by setting $C_0 = -(2C_1 + 2C_y + 2(C_{Az} + C_{Bz}))$ so that the Weyl points where the hole and particle bands touch each other occur at $C = 0$.

The Weyl points of Eq. (1) correspond to the points in k -space where the coefficients of σ_x , σ_y , and σ_z simultaneously vanish. Denoting these points as $\vec{k}_0 = (k_{x0}, k_{y0}, k_{z0})$, we have

$$C_1 \sin(k_{x0}) = 0, \quad (2)$$

$$(C_{Az} - C_{Bz}) \cos(k_{z0}) = 0, \quad (3)$$

$$C_1(1 + \cos(k_{x0})) + C_y(2\cos(k_{y0})) = 0. \quad (4)$$

Equation (2) implies that $k_{x0} = \pi$. ($k_{x0} = -\pi$ is also a solution of Eq. (2), but $k_{x0} = \pm\pi$ are equivalent if we set the Brillouin zone boundaries at $\pm\pi$.) Equation (3) implies that $k_{z0} = \pm\pi/2$. Substituting the values of k_{x0} and k_{z0} into Eq. (4) gives $k_{y0} = \pm\pi/2$. There are therefore four inequivalent Weyl nodes located at $(k_{x0}, k_{y0}, k_{z0}) = \pi(1, \eta_y/2, \eta_z/2)$ where η_y and η_z assume values of ± 1 . Considering now the linear expansion of Eq. (1) for a small displacement $\delta\vec{k} = (\delta k_x, \delta k_y, \delta k_z)$ around $\vec{k}_0 = \frac{\pi}{2}(2, \eta_y, \eta_z)$, we

have

$$H(\vec{k}_0 + \delta\vec{k}) = \begin{pmatrix} 2C_1\sigma_x \\ 2\eta_y C_y \sigma_x \\ \eta_z((C_{Az} + C_{Bz})\mathbf{I}_\sigma + (C_{Az} - C_{Bz})\sigma_z) \end{pmatrix} \cdot \begin{pmatrix} \delta k_x \\ \delta k_y \\ \delta k_z \end{pmatrix}. \quad (5)$$

The last term, i.e., the coefficient of δk_z contains a $(C_{Az} - C_{Bz})$ term which is proportional to the Fermi velocity along the k_z direction, and a $(C_{Az} + C_{Bz})\mathbf{I}_\sigma$ term which imparts a tilt to the Dirac cone along the k_z direction. Our TE model will host Type I Weyl nodes as long as the coefficient of σ_z dominates over the coefficient of \mathbf{I}_σ . Conversely, a Type II WSM phase emerges when $|C_{Az} + C_{Bz}| > |C_{Az} - C_{Bz}|$. Moreover, a new topological WSM phase we call the Type III phase emerges at the transition point between the Type I and Type II phases when $|C_{Az} + C_{Bz}| = |C_{Az} - C_{Bz}|$. Summarizing, the conditions for the three WSM phases are

$$|C_{Az} + C_{Bz}| < |C_{Az} - C_{Bz}|, \quad \text{Type I} \quad (6)$$

$$|C_{Az} + C_{Bz}| > |C_{Az} - C_{Bz}|, \quad \text{Type II} \quad (7)$$

$$|C_{Az} + C_{Bz}| = |C_{Az} - C_{Bz}|, \quad \text{Type III} \quad (8)$$

Figure 2 shows the C dispersion relations of an exemplary Type I WSM and Type II WSM modeled by the TE circuit of Fig. 1 with capacitive values $C_1 = 0.716$ mF, $C_y = 0.167$ mF and $C_{Az} = 0.5$ mF, and $C_{Bz} = -0.5$ mF for the Type I WSM and $C_{Bz} = 0.2$ mF for the Type II WSM, respectively. In the respective circuits, the value of C_0 has been set so that the Weyl points occur at $C = 0$. (We chose mF as the unit accompanying the numerical capacitance values used in our calculations because, for the reasonable value of $\omega = 1$ kHz, the inductance corresponding to a given negative numerical value of capacitance in mF has the same (positive) numerical value in μH . Capacitors and inductors with capacitances and inductances on the order of 1 mF and 1 μH , respectively, would have physical dimensions of ≈ 1 cm, and are readily available.)

Figure 2a shows the untilted Type I WSM that results when C_{Az} and C_{Bz} have the same magnitudes, but opposite signs. The low- C dispersion relation takes the familiar form of Dirac cones with ellipsoid cross-sections centered around the four Weyl nodes (see Fig. 2c, d). The gradients of the dispersion relation have opposite signs for opposite signs of δk_y and δk_z around each Weyl node.

Figure 2b shows the Type II WSM that results when C_{Az} and C_{Bz} have the same signs. The equal capacitance contours (ECC, in analogue to the more familiar term “equal energy contours”) are reflection-symmetric about the k_y axis due to the reflection symmetry about the y -axis in the TE circuit. The form of the ECCs in a Type II WSM stands in contrast to the more familiar ellipsoidal cross-sections of the Type I WSM Dirac cones. In the vicinity of a Weyl node, the ECC of a Type II WSM takes the form of a hyperbola with its transverse axis parallel to the tilt direction along the z direction (see inset of Fig. 2b). One branch of the hyperbola corresponds to hole states in the sense that if we write the Hamiltonian as $H = \vec{m} \cdot \vec{\sigma}$, then for an eigenstate on the hole branch, $|h\rangle$, we have $\langle h|\vec{\sigma}|h\rangle = -\vec{m}$. The other branch corresponds to particle-like states where an eigenstate on the branch, $|p\rangle$, yields $\langle p|\vec{\sigma}|p\rangle = \vec{m}$. Unlike the ellipsoid ECCs of a Type I WSM, the hyperbola ECCs of the Type II WSM are not closed curves. The non-closure of hyperbolas and the periodicity of the first Brillouin zone together cause the ECCs to deviate from perfect hyperbolas far away from the projections of the Weyl nodes. In our TE circuit, the hyperbolas around Weyl nodes with

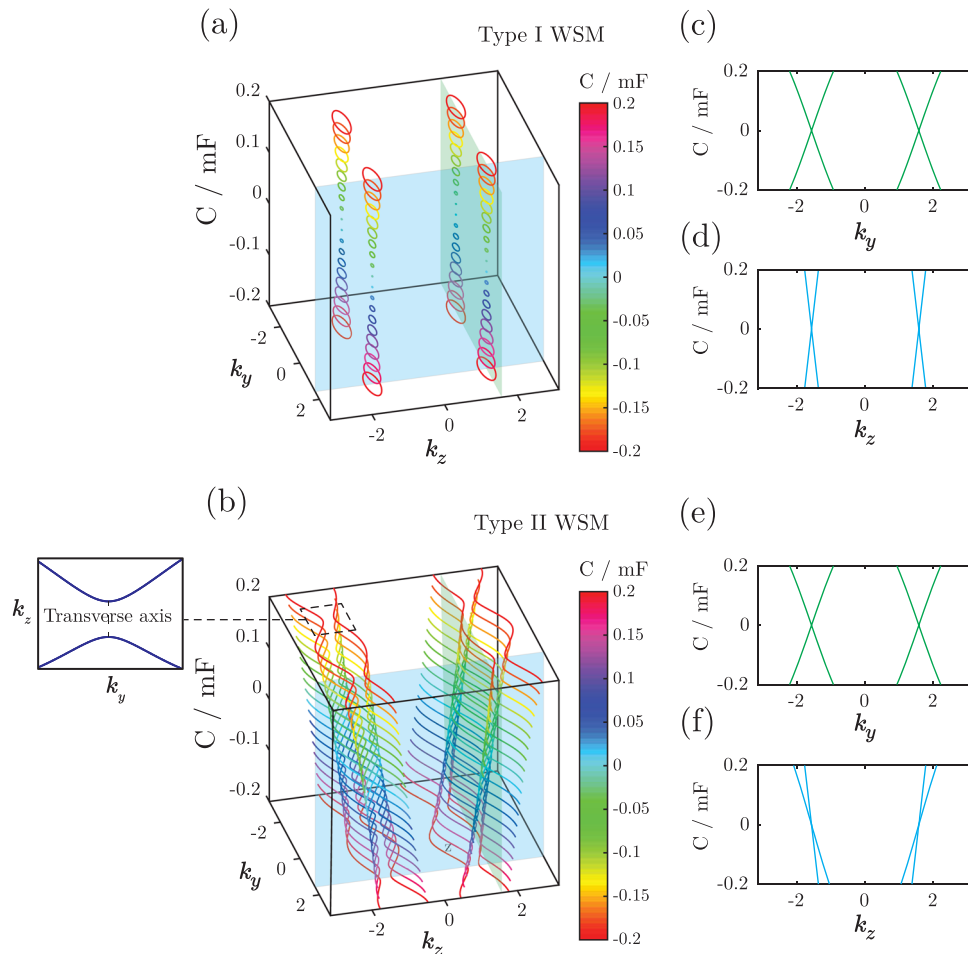


Fig. 2 Dispersion relations of Type I and Type II Weyl semimetal (WSM) phases. The k -space equal-capacitance (C) contours of a topoelectrical (TE) circuit: **a** a Type I WSM and **b** a Type II WSM. The $k_y = \pi/2$ planes are indicated on **(a)** and **(b)**. The inset of **(b)** shows a zoomed-in view of the hyperbolic Equal capacitance contours (ECCs) near one of the Weyl points. **c** and **e** show the C -dispersion relation with k_y at $k_x = \pi$, $k_z = \pi/2$ for the systems in **(a)** and **(b)** respectively; **d** and **f** show their respective C -dispersion relations with k_z at $k_x = \pi$, $k_y = \pi/2$.

the same sign of k_z link up so that the ECCs take the form of lines running along the k_y axis in the Brillouin zone.

Figure 2e, f illustrate an important distinction between a Type II WSM and a Type I WSM. Whereas the gradient of the dispersion relation around each Weyl node has opposite signs for opposite signs of δk_y perpendicular to the tilt direction in both Type I and Type II WSMs, the gradients of the dispersion relations have the same signs for both signs of δk_z parallel to the tilt direction in the Type II WSM. This characteristic property of a Type II WSM will lead to interesting consequences for its transport properties, as we shall see in the next section.

Energy flux transport in Weyl heterojunction. Having constructed the TE circuit equivalent of a TB model of a heterojunction and established the equivalence between the energy flux in the TE circuit with the electron flux in the TB model (details in Supplementary Notes 1 and 2), we are now in a position to study the transport in TE circuit heterojunction analogues of WSMs heterostructure.

We now consider the transport across a heterojunction formed between a Type I and Type II WSMs shown in Fig. 2. The transmission of the energy flux is calculated for an incident mode from a semi-infinite long Type I source lead to a semi-infinite long Type II drain lead. This is the TE analogue of solving for the transmitted current for a given incident source mode in a TB

heterojunction (more details in Supplementary Note 3). In the Landauer–Buttiker picture conventionally used in calculating the conductances across heterojunctions in condensed matter systems, it is assumed that all states in the source lead are populated up to the source Fermi energy. In the limit of small applied source–drain bias, the calculation of the conductance requires the consideration of the contributions from all source states at the Fermi energy propagating from the source to the drain. However, in some cases, it is preferable to limit the conductance contributions to a restricted set of source states at the Fermi energy. For instance, in the case of the Datta–Das spin transistor⁴⁴, the ideal behavior is approached by limiting the conductance contribution to normally incident source states. Thus, experimentally, additional steps have to be taken to exclude the contributions of the unwanted source states. In contrast, the source lead in a TE system can be populated with only a single incident mode by appropriately setting the voltage biases at the source voltage nodes, as explained in Supplementary Note 1. We therefore focus exclusively on the set of source modes with $k_x = \pi$ in the rest of the paper.

We compare the two scenarios where the source–drain interface is parallel, and where the interface is perpendicular to the tilt direction along the z direction. Figure 3 shows the results of an exemplary calculation at $C = 0.1$ mF for a Type I source lead connected to a Type II drain lead with the same parameters as in Fig. 2. Figure 3c, d show the ECCs, and the transmitted energy

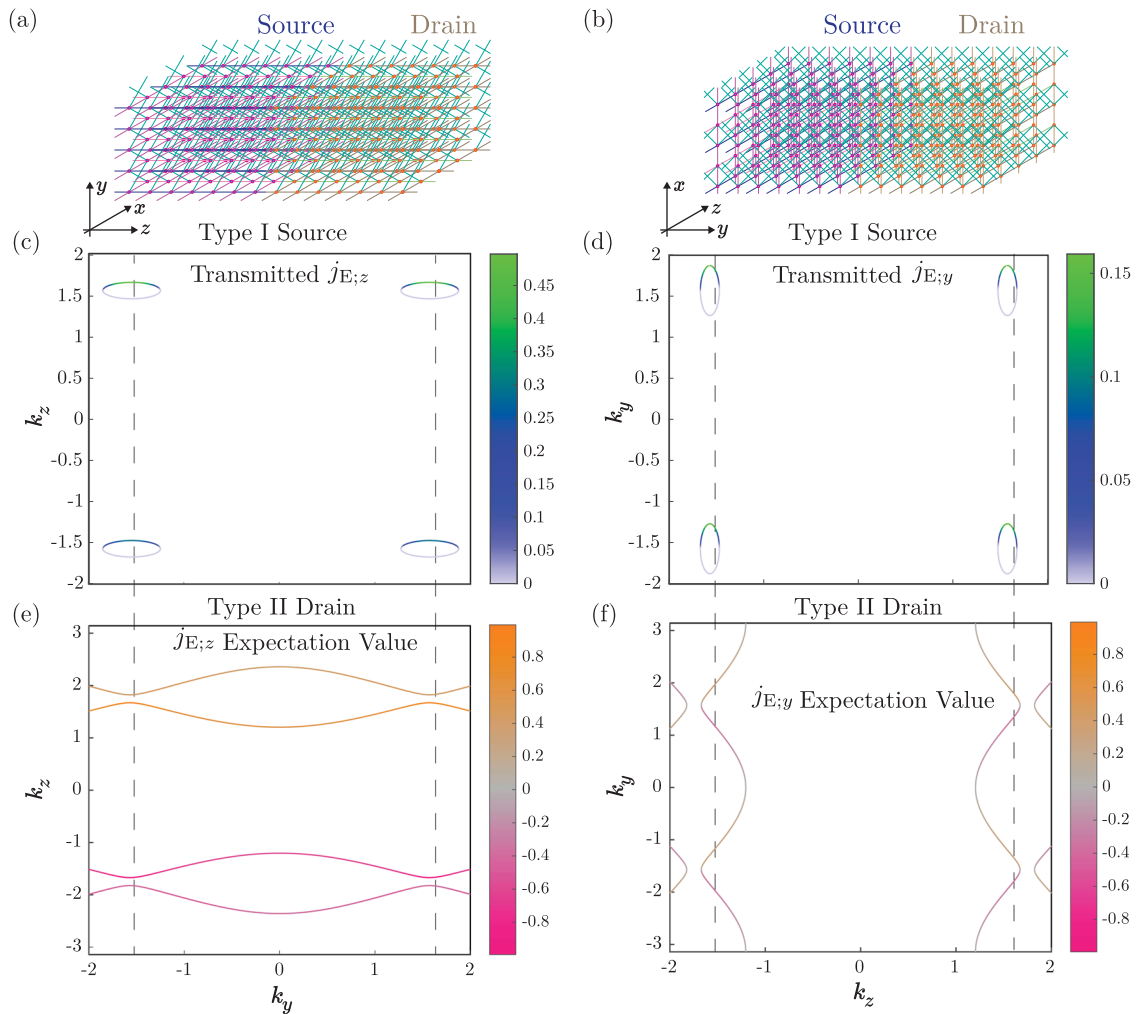


Fig. 3 Transmitted energy flux in a Type I-Type II Weyl semimetal (WSM) heterojunction. **a, b** The three-dimensional schematic diagrams of the topoelectrical (TE) WSM circuits for energy flux propagation along **a** the z and **b** y directions respectively. The dots represent the circuit nodes and the lines the capacitive couplings between the voltage nodes. The unconnected lines at the edges of the circuit indicate that the circuit extends to infinity beyond these lines. **c, d** The $k_x = \pi$ source equal capacitance (C) contours at a fixed common capacitance $C = 0.1$ mF and transmitted energy flux $j_{E;z/y}$ for each mode on the source ECC source incident on the source-drain interface between a Type I source lead and a Type II drain lead for transmission along the **c** z and **d** y directions. **e, f** The expectation values of the drain energy flux along the **e** z and **f** y directions. The vertical lines in **(c-f)** linking the Type I source and a Type II drain indicate points on the source and drain ECCs with the same conserved values of **c, e** k_y , and **d, f** k_z momentum respectively (note that the plot axes are swapped between **(c)** and **(e)**; and **(d)** and **(f)**).

flux at every point on the source ECCs for energy flux flowing in the $+z$ direction (Fig. 3c) and in the $+y$ direction (Fig. 3d). The transmitted energy flux was calculated by finding the linear superposition of source and drain eigenmodes which corresponds to flux incident on the source side, and satisfies the circuit KCL at every node in the circuit (see Supplementary Note 1 for details). The transmitted energy flux is therefore equal to zero on one half of the source ECCs where the flux propagates away from the source-drain interface. Figure 3e, f show the drain ECCs and the energy flux along the z direction (Fig. 3e), and y direction (Fig. 3f) on each point of the ECCs. Denoting the eigenmode with eigenvalue C at \vec{k} as $\mathbf{v}(\vec{k})$, the energy flux along the z and y directions was calculated using $\mathbf{v}(\vec{k})^\dagger (\partial_{k_z/k_y} \mathbf{H}) \mathbf{v}(\vec{k})$, which we refer to as the “expectation value” of the energy flux. We have oriented the axes of the plots so that the momentum perpendicular to the interface, which is conserved across the interface, lies on the horizontal axis of the respective plots. The vertical lines spanning across the middle and bottom plots therefore link the source modes with the corresponding drain

modes which they are transmitted into, subject to the conservation of transverse momentum.

The transmission of the energy flux differs considerably between the scenarios where the transmission direction is parallel to, and when it is perpendicular to the tilt direction. In Fig. 3c, e, where the flux direction is parallel to the tilt direction, the transmitted energy flux for the source valleys with positive k_z is considerably higher than the transmission for the source valleys with negative k_z . The valley asymmetry arises because of the distribution of the z -energy flux directions in the drain segment. At the given value of C , the drain segment hosts only modes which propagate in the $+z$ ($-z$) direction at positive (negative) k_z . This is shown in Fig. 3e as well as in Fig. 2f. The conservation of the transverse momentum k_y restricts incident source modes at the source-drain interface to be transmitted into drain modes with the same value of k_y . This implies that source modes at the negative k_z valley have to undergo inter-valley scattering into the positive k_z drain valley in order to be transmitted into drain modes which propagate in the positive z direction away from the interface. The large difference Δk_z between the incident source

mode and transmitted drain mode involved in the inter-valley scattering suppresses the transmission of source modes at the negative k_z valleys relative to those at the positive k_z valleys. For the positive k_z source valley, the required Δk_z in the intra-valley scattering between the source and drain modes is much smaller.

The preferential transmission of energy flux for the positive k_z valleys vanishes when the transmission direction (along y) is perpendicular to the tilt direction (along z). The transmitted energy flux in Fig. 3d, f for propagation along the $+y$ direction has identical profiles in all four valleys, i.e., they are valley independent. Here, for a given conserved value of k_z , drain modes propagating in the $+y$ direction are present symmetrically around the vicinity of all four Weyl nodes. The source modes incident from all four valleys do not have to undergo inter-valley scattering in the drain segment in order to be transmitted in the forward $+y$ direction.

A key distinction between a Type I WSM and a Type II WSM is that in the former (latter), there exists states in the vicinity of a Dirac point with both signs (one sign) of energy flux parallel to the tilt direction. This implies that at the transition from a Type I WSM to a Type II WSM, some of the states will have zero energy flux along the tilt direction. Let us consider the transition from a Type I to a Type II WSM. From Eq. (7), this transition occurs at $C_{Bz} = 0$. In this special case, the C dispersion relation of Eq. (5) takes the form of $C = \eta_z(1 \pm 1)C_{Az}\delta k_z$ where the \pm indicates the pseudospin branch of the eigenvalue. C does not disperse with δk_z for the negative pseudospin branch. We term this transitional regime between a Type I and Type II WSM as Type III WSM.

Figure 4a shows the ECCs of a Type III WSM system, and the k_y and k_z dispersion relations cutting across the Weyl nodes (see Fig. 4b, c). Figure 4c shows that one of the branches of the cross-section of the Dirac cone now lies flat parallel to the k_z axis, in agreement with our prediction earlier from the linear expansion of $\delta \vec{k}$ around the Weyl points in Eq. (5). The flatness of one of the eigenspinor branches means that for $k_x = \pi$ and $C \neq 0$, a line of constant k_y cuts across the C dispersion of Type III WSM at two points instead of four points in the case of Type II WSM. Furthermore, the ECC profile in Fig. 4a for a Type III WSM consists of only two curves across the k_y range spanned by the Brillouin zone, instead of the four curves for a Type II WSM in Fig. 2b. The absence of states from one of the eigenspinor branches leads to a qualitative difference for the transmission from a Type I WSM source lead to a Type III WSM drain lead, compared to the transmission from a Type I WSM source lead to a Type II drain lead. In what follows, we consider only the positive k_y valleys because the reflection symmetry of the TE system along the y direction results in the other pair of valleys with $k_y < 0$ having identical transmission profiles as their y reflection partners.

Figure 4d–g plot the transmission from the positive k_y , positive k_z source valley (see Fig. 4d, f) and positive k_y , negative k_z source valley (see Fig. 4e, g), from a Type I WSM source to a Type II WSM drain (Fig. 4d, e), and to a Type III WSM drain (Fig. 4e, f) with the same parameters as in Fig. 4a, as a function of the common capacitance C and the incidence angle ϕ_z . An incidence angle of zero corresponds to normal incidence at the interface. For both Type II and Type III drain leads, the transmitted flux $j_{E,z}$ is higher for incident modes from the positive k_z valley than that from the negative k_z valley. The suppressed transmission of the negative k_z valley source modes is, in both cases, due to the inter-valley scattering into positive k_z valley drain states required for transmission from the source to the drain. (The k_z dispersion relation in Fig. 4c shows that in the vicinity of each Weyl point there are only modes with a single sign of $\partial_{k_z} C$, which signifies the

energy flux along the z direction.) However, a key difference between the transmission to a Type II drain as opposed to a Type III drain is that in the former, the transmission for the negative k_z state is maximal at normal incidence at $k_z = 0$ whereas in the latter, the transmission of the negative k_z states at normal incidence is completely suppressed. This complete suppression of the transmission at normal incidence is, in a sense, the antithesis of the well-known Klein tunneling in Dirac fermion systems. We term this tunneling behavior as “anti-Klein tunneling”. The emergence of anti-Klein tunneling is basically due to the fact that propagating states exist in only one eigenspinor branch around each Weyl point in a Type III WSM.

To further explain the existence of the anti-Klein tunneling behavior, let us consider Fig. 5 which shows the ECCs in the source (see Fig. 5a, c) and drain (see Fig. 5b, d) for a Type III WSM drain lead (Fig. 5a, b), and a Type II WSM drain lead (Fig. 5c, d), and the expectation value of the pseudospin σ_z at each point of the ECC. The modes which propagate in the positive z direction from the source to the drain (the right halves of the elliptical ECCs in the Type I source, and the positive k_z curves in the Type II and Type III drains) are demarcated in dotted red boxes in the figure. As noted earlier in the discussion on Fig. 4, the Type III ECCs at any non-zero value of C consist of only two curves running along the k_y axis, both of which belong to the $+\sigma_z$ eigenspinor branch. The normal incidence of the source mode from each valley at $\phi_z = 0$ corresponds to the conserved values of $\delta k_x = \delta k_y = 0$ around each Weyl point in both the source and drain segments in the linear $\delta \vec{k}$ expansion Eq. (5). At normal incidence and $C_{Bz} = 0$, Eq. (5) reduces to $H = C_{Az}\eta_z\delta k_z(\mathbf{I}_\sigma + \sigma_z)$. Since the given value of $C > 0$, $2C_{Az}\eta_z\delta k_z > 0$. The sign of the pseudospin z expectation value of the $+\sigma_z$ eigenstate follows that of $C_{Az}\eta_z\delta k_z$. The pseudospin about the Weyl points at $\delta k_x = \delta k_y = 0$ would thus lie along the $+z$ direction for all four drain valleys in Type III WSM, as shown in Fig. 5b. This matches the σ_z direction of the normally incident source states from the positive k_z valleys (Fig. 5a), which thus get transmitted perfectly (transition (1) in Fig. 5). However, the normally incident source states from the negative k_z valleys have pseudospin σ_z along $-z$, i.e., in the opposite direction to that of the drain states. In other words, the source and drain states at normal incidence are orthogonal to one other as far as their pseudospin state is concerned. This leads to a total suppression of the transmission of normally incident states, i.e., “anti-Klein tunneling” (the forbidden transition (2)). In conventional Klein tunneling with coincident source and drain Dirac points, there is perfect transmission because the pseudospin directions of the source and drain states point in exactly the same direction regardless of the potential difference between the source and drain. In contrast, in our TE (Type I–Type III) heterojunction system, the pseudospin direction of the normally incident source states at the negative k_z valley points in the exactly opposite direction to that of the corresponding drain states, thus resulting in zero transmission.

In contrast to the Type III WSM drain segment of Fig. 5a, b, the Type II drain segments in Fig. 5c, d have states from both eigenspinor ($\sigma_z = \pm 1$) branches present at all four Weyl points. The transmission of normally incident modes from the negative k_z valley to the forward propagating drain modes in the positive σ_z branch (the forbidden transition (3)) is prohibited due to their respective pseudospins pointing in opposite directions. However, it is possible for the source modes to be transmitted into the drain modes in the $\sigma_z = -1$ branch. Indeed at normal incidence, the pseudospin directions of the source modes and the corresponding drain modes in the $-\sigma_z$ branch point in exactly the same direction, resulting in the valley transmission peaking at $\phi_z = 0$

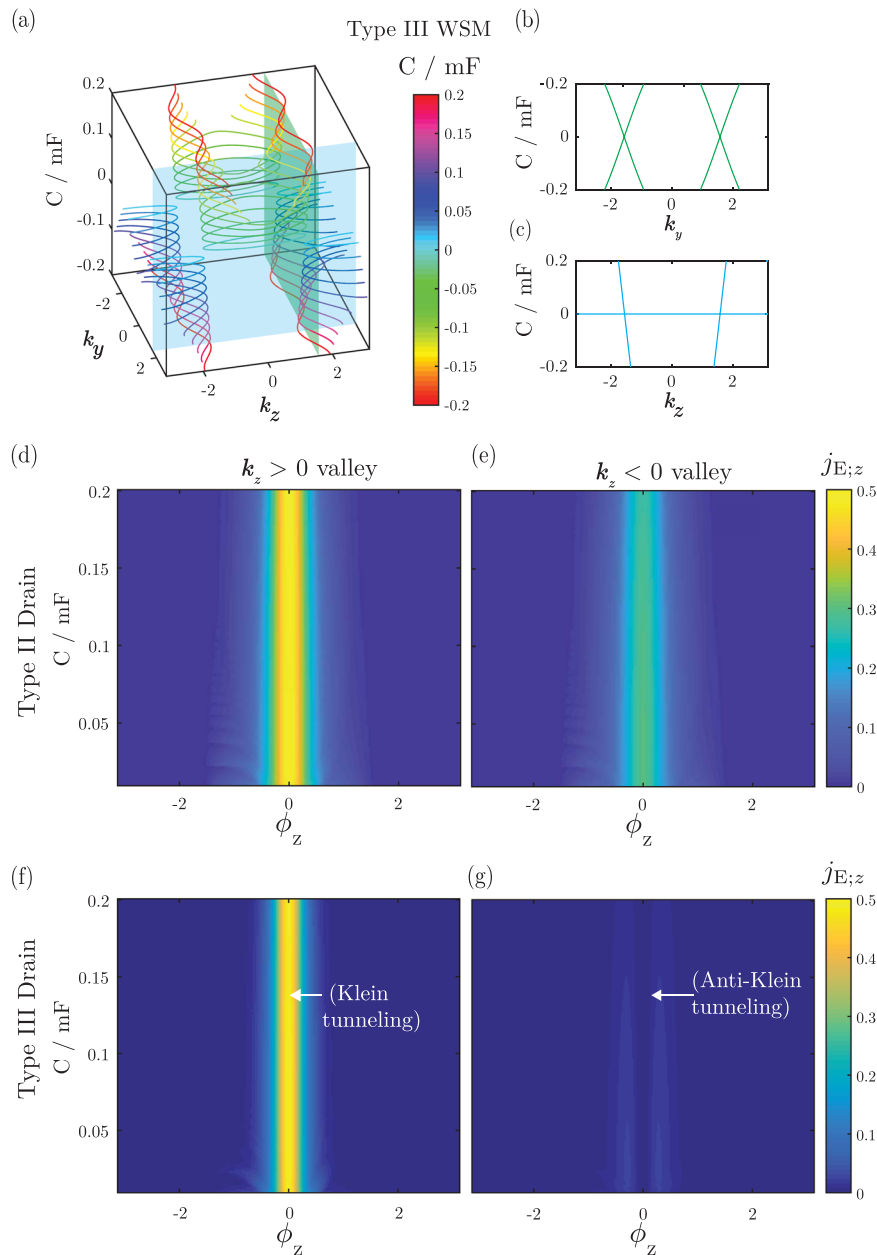


Fig. 4 Energy flux transmission in a Type I-Type III Weyl semimetal (WSM) heterojunction. **a** The equal capacitance contours (ECCs) for a Type III WSM at $k_x = \pi$ with the $k_z = \pi/2$ and $k_y = \pi/2$ planes indicated, **b** the C-dispersion relation with k_y at $k_z = \pi/2$, and **c** C-dispersion relation with k_z at $k_y = \pi/2$. **d** and **e** show the variation of the transmitted energy flux $j_{E;z}$ with the common grounding capacitance C and incidence angle ϕ_z valley from a Type I source from the positive k_z , **d** positive k_z valley and **e** negative k_z to a Type II WSM drain. **f** and **g** show the transmissions from the positive and negative k_z valleys from a Type I source to a Type III drain, respectively.

for the $-k_z$ valley (transition (4)). However, since inter-valley scattering is involved in the transmission, the transmission probability T is somewhat suppressed, in contrast to the perfect transmission in conventional Klein tunneling.

Discussion

In this work, we established the analogy between a TE circuit and a TB system. We saw that the common grounding capacitance and the energy flux in the former are analogous to the eigenenergy and the probability flux in the latter. We also described how multi-dimensional heterojunctions between semi-infinite leads may be modeled using a finite number of nodes.

Exploiting the analogy between LC TE circuits and TB Hamiltonians, we proposed the realization of various WSM

phases to construct a WSM heterojunction between a Type I WSM source and a Type II/III WSM drain. A TE circuit offers additional flexibility and tunability over a condensed matter system where in the former, a source lead can be populated with a specific mode by adjusting the voltage bias appropriately. In contrast, in a condensed matter system, the conductance is contributed by all source states at the source Fermi energy, and it is difficult to restrict the conductance to a desired subset of source modes. We saw that the transport properties differ significantly for the cases when the transport direction is parallel to, and when it is perpendicular to the k -space tilt direction. By investigating the relative orientation between tilt and flux direction, we observed that large inter-valley scattering suppresses the transmission for one pair of source valleys relative to the other when

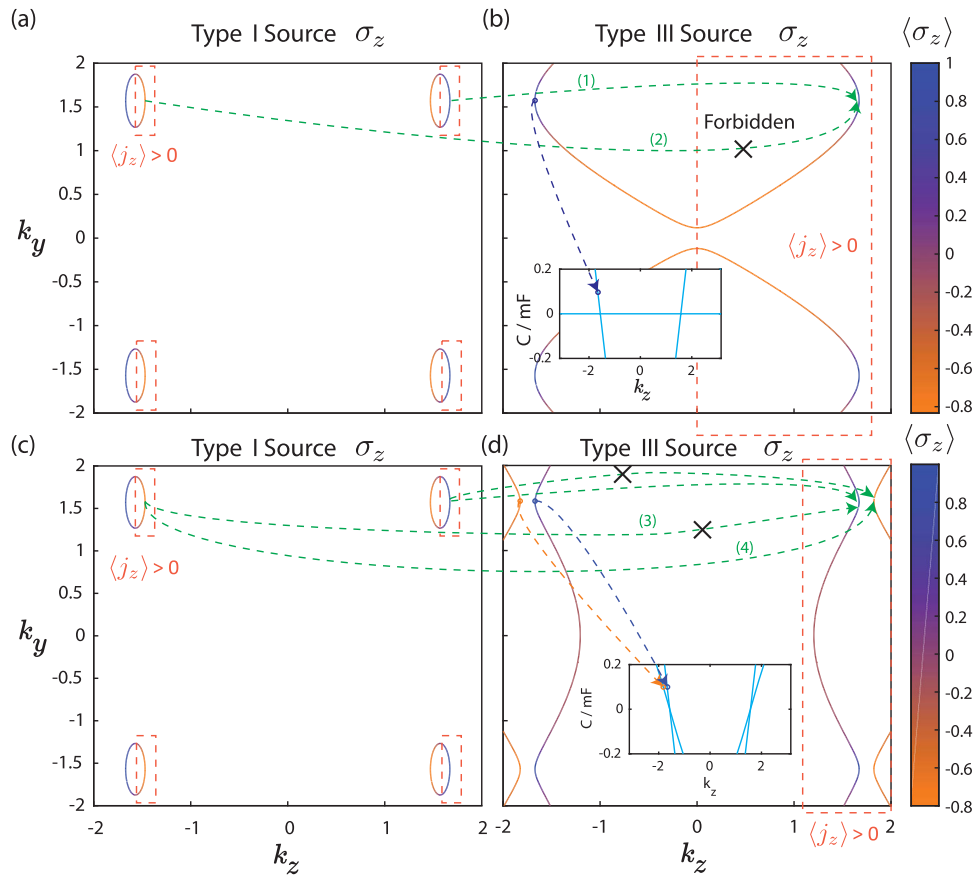


Fig. 5 Equal capacitance contours (ECCs) in source and drain. **a–d** The ECCs and the expectation value of pseudospin $\langle \sigma_z \rangle$ at each mode on the ECCs in **a**, **c** Type I source, **b** Type II drain, and **d** Type III drain at $C = 0.1$. The red dotted boxes denote the modes with energy fluxes in the positive z direction. The dotted arrows spanning across the source and drain ECCs at $k_y = \pi/2$ denote the drain states that the normal incident $\phi_z = 0$ source states can be transmitted into. The insets in **(b)** and **(d)** relate the ECC curves to bands on the C – k_z dispersion relation. The labels (1)–(4) denote various allowed and forbidden transmission processes from the positive k_y , $\delta k_y = \delta k_x = 0$ source modes in the two valleys to the forward-propagating drain modes.

the tilt and flux direction are parallel to each other. However, all valleys contribute equally in transmission when the tilt direction is perpendicular to the propagation direction. Moreover, by adjusting the coupling capacitance, we achieved an exotic Type III WSM drain lead where one of the eigenspinor branches shows zero group velocity along the tilt direction. The flatness of Type III WSM band dispersion results in anti-Klein tunneling where the transmission for the negative k_z valleys at normal incidence is totally suppressed. This is due to the pseudospin directions of the source and drain modes pointing in exactly opposite directions, leading to the orthogonality of the source and drain pseudospin states. Moreover, transmission characteristics such as Klein and anti-Klein phenomena in WSM heterojunction show robustness against system disorders such as parasitic resistance, capacitance or inductance. (See details in Supplementary Note 4.)

Our proposed model can be easily implemented experimentally with conventional electrical components. Realizing various WSM phases in a single real material is difficult to achieve in practice. Moreover, the transmission across a heterojunction separating different phases of WSM (i.e., Types I, II, and III) has unique characteristics which can be utilized in WSM-based nanoelectronics (e.g., to realize valleytronic applications). We thus propose the TE circuit network analogue of a WSM heterojunction as a platform to study the transport behavior of WSM materials.

Methods

Hamiltonian analogue. We explain how to establish the analogy between an inductance–capacitance (LC) circuit, and the quantum mechanical TB

Hamiltonian. In complex circuit theory, the complex current I flowing through a LC component is given by $I = Y\delta V$ where Y is the admittance of the component, and δV is the potential difference across the component. The admittance of a capacitor with capacitance C for a harmonic AC current of angular frequency ω is $Y_C = i\omega C$, while that of an inductor with inductance L is $Y_L = -\frac{i}{\omega L}$. From the perspective of admittance, an inductor therefore behaves like a capacitor with a negative capacitance, with the induction corresponding to a negative capacitance $-|C|$ given by $|L^{-1}| = (\omega^2)|C|$. In the rest of this paper we shall, for simplicity refer to capacitors and capacitance exclusively with the understanding that a negative capacitance actually refers to an inductance.

To set the stage, let us consider a very simple system illustrated in Fig. 6a, consisting of two circuit nodes numbered 1 and 2 connected by identical capacitors C to the ground. The two nodes are connected by a capacitor C_i . (The i in the subscript is not to be interpreted as a dummy index.) An ideal voltage source sets the voltage bias at node 1 to V_1 with respect to the ground. We denote the current flowing through the voltage supply as I^{VS} .

In general, the total current flowing into the n th voltage node in a circuit composed purely of capacitors (and inductors), I_n , is given by

$$I_n = (i\omega) \sum_a C_{an}(V_n - V_a)$$

where the sum runs over all the nodes which node n is connected to via the coupling capacitances C_{an} . By Kirchhoff's current law (KCL), the net current flowing into any voltage node is 0. We therefore have

$$0 = \sum_a C_{an}(V_n - V_a) - \frac{I_n^E}{i\omega} \quad (9)$$

where I_n^E accounts for any additional current flows out of the n th node besides those due to capacitors connected to the node. In the circuit in Fig. 6a, $I_1^E = I^{VS}$, $I_2^E = 0$.

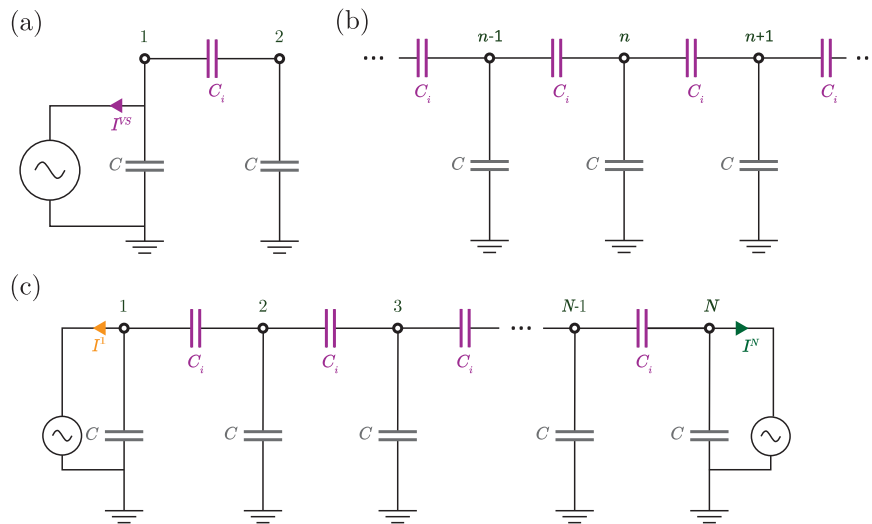


Fig. 6 Electrical circuit to resemble quantum tight binding model. **a** Schematic of a two-node circuit consisting of two voltage nodes connected to the ground via identical capacitances C , and connected to each other via a coupling capacitance C_i . A voltage source is connected to node 1 with the current flowing through the voltage source denoted as I^{VS} . **b** Schematic of an infinite chain of voltage nodes coupled to each other with coupling capacitances C_i and connected to the ground via common capacitances C . **c** Schematic of a finite chain of voltage nodes equivalent to the infinite chain in **(b)**, consisting of the chain truncated to N nodes and voltage supplies attached to both ends of the finite chain.

Applying Eq. (9) to the two nodes in Fig. 6a, we have

$$C \begin{pmatrix} V_1 \\ V_2 \end{pmatrix} = C_i \begin{pmatrix} -1 & 1 \\ 1 & -1 \end{pmatrix} \begin{pmatrix} V_1 \\ V_2 \end{pmatrix} + \frac{i}{\omega} \begin{pmatrix} I^{VS} & 0 \\ 0 & 0 \end{pmatrix}. \quad (10)$$

Equation (10) looks almost like an eigenvalue equation for the matrix $C_i(-\mathbf{I}_2 + \sigma_x)$ with eigenvalues C and eigenvector $(V_1, V_2)^T$ if not for the second term containing the current flowing through the voltage supply. (\mathbf{I}_2 is the two-by-two identity matrix and σ_x is the x Pauli matrix.) We can ask the question of what values C should take for a given value of C_i , so that the current flowing through the voltage supply is zero. This question is answered by setting $I^{VS} = 0$ in Eq. (10), so that Eq. (10) takes the form of

$$C\mathbf{v} = C_i(-\mathbf{I}_2 + \sigma_x)\mathbf{v} \quad (11)$$

where bold uppercase symbols denote matrices and bold lowercase symbols vectors. Here \mathbf{v} is the vector of the voltages at the nodes. Equation (11) can readily be diagonalized to give the eigenvalues $C = C_i(1 \pm 1)$. Notice that once the C capacitances are set to $C_i(1 \pm 1)$ and the voltage bias supplied by the voltage supply V_1 set to an arbitrary value, Kirchhoff's laws automatically guarantee that the voltage at node 2 will be $\pm V_1$.

Equation (11) is the TE analogue of a quantum-mechanical TB Hamiltonian consisting of only two lattice sites with on-site energy $-C_i$ and hopping integral C_i . More generally, TE analogues to quantum TB Hamiltonians can be extended to any number of lattice sites. In these TE analogues, the voltage nodes connected to the ground via the capacitance C play the role of TB lattice points while the capacitive (and inductive) couplings between lattice sites play the role of TB hopping integrals. Hence, the voltage profile across the nodes in a TE circuit is analogous to the spatial variation of the wavefunction in a TB system while C stands in for the eigenenergy. For a finite one-dimensional chain with only nearest-neighbor couplings, the chain can be populated with a desired eigenmode by attaching a voltage supply at one of the voltage nodes. Generalizing Eq. (11), we write

$$C\mathbf{v} = \mathbf{H}\mathbf{v} \quad (12)$$

where \mathbf{H} is the TE analogue of the TB Hamiltonian obtained from writing down the KCL at every node, moving the terms containing the capacitance C to the left of the equal sign and setting the current flowing through the attached voltage supply to zero. We want the current through the voltage supply to be zero by design, because otherwise a finite current flow will contribute an imaginary on-site potential energy term into \mathbf{H} , an example of which is the $-I^{VS}/i\omega$ term in Eq. (10). The imaginary on-site potential energy term breaks the Hermiticity of \mathbf{H} . Imposing the current through the voltage supply to be zero ensures that the voltage supply does not introduce any additional terms into \mathbf{H} , and can thus be attached to any of the voltage nodes without affecting the form of \mathbf{H} . The eigenvalues of \mathbf{H} hence correspond to the allowed values of C in which the current flowing through the voltage supply is indeed zero. We stress that although no current flows through the voltage supply when C is set to one of the eigenvalues, the physical scenario is not equivalent to simply removing the voltage supply and leaving the circuit open. The AC voltage supply imposes a finite $\frac{dV}{dt}$ at the node it is attached to. The finite temporal rate of change of the potential differences across the capacitors in the circuit leads to the charging or discharging of these capacitors and the flow of

electrical currents through them even though the current through the voltage source is zero.

Let us briefly summarize what we have done so far. We saw that the TE analogue Eq. (12) to the Schrodinger's equation $E|\psi\rangle = H|\psi\rangle$ can be established by considering the KCL at the voltage nodes of a LC circuit. The voltage profile vector \mathbf{v} is the TE analogue of the wavefunction while C , the common grounding capacitance for all the nodes, plays the role of the eigenenergy. In finite TE circuits analogous to finite TB systems, the eigenvalues of C correspond to the values of common grounding capacitances for which no current flows through a voltage supply attached to any node. (The voltage supply serves to populate the voltage nodes with finite voltages.) The fact that no current flows through the voltage supply for an eigenvalue of C allows us to attach the voltage supply to any node without modifying \mathbf{H} and the voltage profile of the eigenmodes.

Infinite one-dimensional chains. Building towards our goal to study heterojunctions between semi-infinite leads, let us now move on from finite circuits and consider the infinite one-dimensional chain shown in Fig. 6b. Each node is connected to its immediate neighbors to the left and right by a coupling capacitance C_i , and connected to the ground via the common grounding capacitance C . Writing down the KCL for the n th node, we have

$$CV_n = C_i(V_{n+1} + V_{n-1} - 2V_n). \quad (13)$$

This is a recursive relation in V_n . Substituting the ansatz that $V_n = v_0 \exp(ikn)$ into Eq. (13), we have $C = 2C_i(\cos(k) - 1)$, which gives $k = \kappa \equiv \arccos(\frac{C}{2C_i} + 1)$. For a given value of C_i , modifying the value of C allows us to modify the spatial wavelength of the voltage profile $2\pi/\kappa$. Notice that both $V_n = v_0 \exp(ikn)$ and $V_n = v_0 \exp(-ikn)$ satisfy Eq. (13). The voltage profile of an eigenmode of the infinite chain thus has the general form of

$$V_n = \alpha_+ \exp(ikn) + \alpha_- \exp(-ikn) \quad (14)$$

where α_{\pm} are the weightages of the $\exp(\pm ikn)$ eigenmodes. This is the TE analogue of a one-dimensional free electron gas system with C playing the role of the eigenenergy. Unlike in a finite chain where a specific eigenmode can be populated simply by setting C to the eigenvalue corresponding to the desired eigenmode and connecting a voltage supply to any one of the nodes, it turns out that the voltage profile in an infinite chain would not be uniquely specified by attaching a finite number of voltage biases to the nodes. (Details in Supplementary Note 5.) The ability to controllably populate desired linear superpositions of eigenstates is an important requirement in setting the direction of flux flowing along a TE heterojunction—we want to populate the eigenmodes such that the TE analogue of probability flux flows only from the source to the drain and not vice-versa. (We discuss the TE analogue to probability flux in Supplementary Note 3.) Moreover, infinitely long chains cannot be constructed in actual experiments. For practical purposes, it is necessary to represent an infinite or semi-infinite circuit by an equivalent circuit comprising a finite number of nodes.

In the following, we construct a chain with a finite number of nodes in which the voltage profile in the interior has an identical form to that in an infinite chain as given by Eq. (14). This is, as we shall later see, sufficient to model the transmission

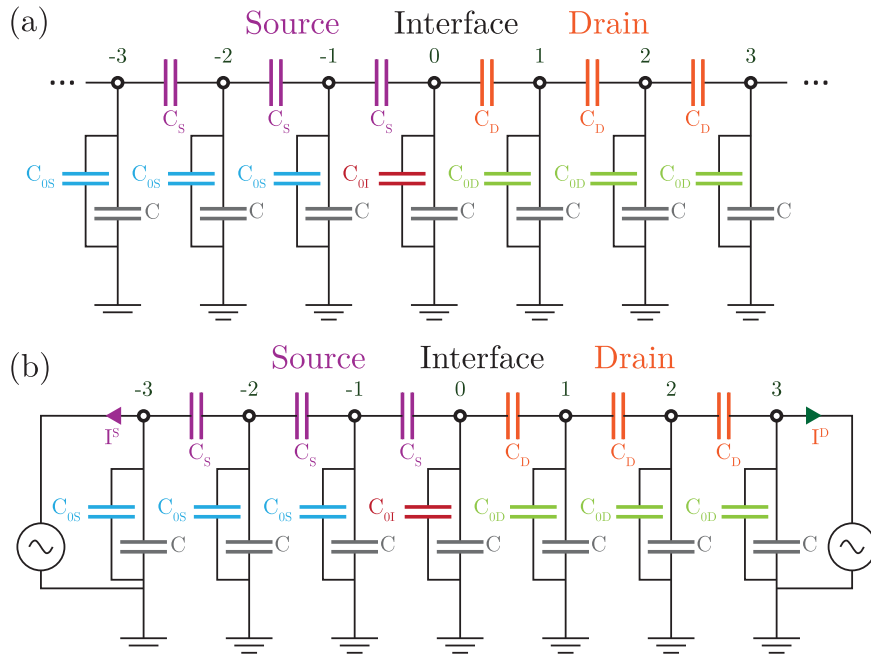


Fig. 7 Topoelectrical heterojunction. **a** Schematic of a heterojunction between a semi-infinite source lead consisting of nodes coupled to their left and right neighbors by a capacitance C_s and to the ground via the common grounding capacitance C and the “on-site energy” C_{0s} , and a semi-infinite drain lead consisting of nodes coupled to their left and right neighbors by a capacitance C_d and to the ground via the common grounding capacitance C and “on-site energy” C_{0d} . **b** Schematic of a finite length chain to model the transmission through the infinite chain consisting of the source and drain leads truncated at the third node away from the interface, and voltage supplies attached to both ends of the system.

from a semi-infinite long source lead to a semi-infinite long drain lead in a heterojunction system.

Figure 6c shows the finite-length chain which can be used to model the homogenous infinite-length chain in Fig. 6b. The finite-length chain is essentially the latter truncated to a finite number of nodes, N , where we now attach voltage supplies to each of the two ends. We number the nodes from 1 to N , and allow finite current flows through the voltage supplies. We denote the currents flowing through the voltage supply at node 1 (N) as I^1 (I^N). Consider nodes 2 to $N - 1$. Each of these nodes is coupled to its left and right neighbors by C_i , and to the ground via the common grounding capacitance C . The KCLs for these nodes take the same form as the KCLs for the infinite chain Eq. (13) for $2 \leq n \leq N - 1$. The voltage profile in these nodes therefore also takes the same form as Eq. (14) for the infinite chain. The finite chain models the infinite chain in the sense that the voltages in the interior nodes in the former are governed by the same Hamiltonian H as the latter and have the same voltage profiles as the infinite chain eigenmodes. The required voltage profile in the finite chain can be obtained by setting the voltage biases at the two ends at appropriate values as will be explained below.

Let us now examine how the weights of the $\exp(\pm ikn)$ modes inside the chain, α_{\pm} , are related to the voltage biases V_1^1 and V_N^N set by the voltage supplies at the two ends. At node 1, the KCL reads

$$CV_1 + \frac{I^1}{i\omega} = C_i(V_2 - V_1) \tag{15}$$

$$= C_i(\alpha_+ \exp(2ik) + \alpha_- \exp(-2ik) - V_1) \tag{16}$$

where in going from Eq. (15) to Eq. (16), we made use of the fact that V_2 is described by Eq. (14). Similarly, at node N the KCL reads

$$CV_N + \frac{I^N}{i\omega} = C_i(\alpha_+ \exp((N - 1)ik) + \alpha_- \exp(-i(N - 1)\kappa) - V_N). \tag{17}$$

At node 2, the KCL reads

$$CV_2 = C_i(V_1 + V_3 - 2V_2)$$

$$\Rightarrow (C + 2C_i)(s_+ \exp(2ik) + s_- \exp(-2ik)) - C_i(V_1 + s_+ \exp(3ik) + s_- \exp(-3ik)) = 0 \tag{18}$$

where again V_2 and V_3 take the form as described by Eq. (14).

In a similar vein, we have at node $N - 1$,

$$(C + 2C_i)(s_+ \exp(i(N + 1)\kappa) + s_- \exp(-i(N + 1)\kappa)) - C_i(V_N + s_+ \exp(i(N - 2)\kappa) + s_- \exp(-i(N - 2)\kappa)) = 0. \tag{19}$$

Equations (16)–(19) constitute a system of four equations relating the six variables $V_{1(N)}$, $I^{1(N)}$, and α_{\pm} to one another. These equations may be interpreted

in two complementary ways. In the first, we take V_1 and V_N as given values and solve for α_{\pm} and $I^{1(N)}$. This corresponds to setting the voltage biases at the two ends of the chain to the given values, and finding out what linear superposition of the $\exp(\pm ikn)$ modes result inside the chain. Alternatively, we can take α_{\pm} to be given, and solve for $V_{1(N)}$ and $I^{1(N)}$. This corresponds to finding out what voltage biases need to be set at the ends of the chain in order to achieve the desired linear superposition of the $\exp(\pm ikn)$ modes inside the chain.

Note that a key difference between the finite length chains in Fig. 6a, c is that we have restricted the current flow through the voltage supply to zero in the former. This is equivalent to setting a hard-wall boundary condition at the ends of the finite chain. The circuit in Fig. 6a is hence the TE analogue of a discretized infinite potential well where the eigenspectrum consists of a discrete set of eigenvalues. In contrast, allowing finite currents to flow through the voltage supplies at the ends of the chain in Fig. 6c is equivalent to setting open boundary conditions at those ends. With reference to the non-equilibrium Green’s function formalism, the imaginary potentials at nodes 1 and N resulting from the current flows through the voltage supplies can be taken to be the imaginary parts of the lead self-energies⁴⁵ at the two ends of a central barrier region attached to semi-infinite leads. The imaginary potentials allow a finite-sized chain to model an infinite-sized one by folding the effects of the portions of the infinite-dimensional Hamiltonian excluded in the former into non-Hermitian terms. The C eigenvalues therefore fall into a continuum. A corollary result is that a semi-infinite chain can be modeled by attaching a voltage source to only one end of a finite chain. This allows the modeling of a TB heterojunction consisting of a semi-infinite source lead connected to a semi-infinite long drain lead, such as the one shown in Fig. 7a.

The fact that an infinite chain can be modeled by a finite one allows us to model the transmission from a semi-infinite source lead to a semi-infinite drain lead across a heterojunction using a finite number of nodes. Figure 7a shows one such heterojunction circuit with semi-infinite leads, and Fig. 7b, the finite-length circuit to model the infinite heterojunction system of Fig. 7a (see Supplementary Notes 1 and 2 for detailed derivations of one-dimensional and multi-dimensional heterojunction).

Data availability

The data that support the plots within this paper and other findings of this study are available from the corresponding author upon reasonable request.

Code availability

The computer codes used in the current study are accessible from the corresponding author upon reasonable request.

Received: 13 September 2019; Accepted: 15 March 2020;

Published online: 30 April 2020

References

- Lu, L., Joannopoulos, J. D. & Soljačić, M. Topological photonics. *Nat. Photonics* **8**, 821 (2014).
- Lu, L., Joannopoulos, J. D. & Soljačić, M. Topological states in photonic systems. *Nat. Phys.* **12**, 626 (2016).
- Süsstrunk, R. & Huber, S. D. Observation of phononic helical edge states in a mechanical topological insulator. *Science* **349**, 47–50 (2015).
- Rocklin, D. Z., Chen, B. G., Falk, M., Vitelli, V. & Lubensky, T. Mechanical Weyl modes in topological Maxwell lattices. *Phys. Rev. Lett.* **116**, 135503 (2016).
- Li, X., Zhao, E. & Liu, W. V. Topological states in a ladder-like optical lattice containing ultracold atoms in higher orbital bands. *Nat. Commun.* **4**, 1–6 (2013).
- Goldman, N., Budich, J. C. & Zoller, P. Topological quantum matter with ultracold gases in optical lattices. *Nat. Phys.* **12**, 639–645 (2016).
- Krishnamoorthy, H. N., Jacob, Z., Narimanov, E., Kretzschmar, I. & Menon, V. M. Topological transitions in metamaterials. *Science* **336**, 205–209 (2012).
- Gao, W. et al. Topological photonic phase in chiral hyperbolic metamaterials. *Phys. Rev. Lett.* **114**, 037402 (2015).
- Peterson, C. W., Benalcazar, W. A., Hughes, T. L. & Bahl, G. A quantized microwave quadrupole insulator with topologically protected corner states. *Nature* **555**, 346–350 (2018).
- Imhof, S. et al. Topoelectrical-circuit realization of topological corner modes. *Nat. Phys.* **14**, 925–929 (2018).
- Lee, C. H. et al. Topoelectrical circuits. *Commun. Phys.* **1**, 1–9 (2018).
- Burkov, A. & Balents, L. Weyl semimetal in a topological insulator multilayer. *Phys. Rev. Lett.* **107**, 127205 (2011).
- Lv, B. et al. Experimental discovery of Weyl semimetal TaAs. *Phys. Rev. X* **5**, 031013 (2015).
- Xu, S.-Y. et al. Discovery of a Weyl fermion semimetal and topological Fermi arcs. *Science* **349**, 613–617 (2015).
- Li, Y. et al. Negative magnetoresistance in Weyl semimetals NbAs and NbP: intrinsic chiral anomaly and extrinsic effects. *Front. Phys.* **12**, 127205 (2017).
- Huang, X. et al. Observation of the chiral-anomaly-induced negative magnetoresistance in 3d Weyl semimetal TaAs. *Phys. Rev. X* **5**, 031023 (2015).
- Wan, X., Turner, A. M., Vishwanath, A. & Savrasov, S. Y. Topological semimetal and Fermi-arc surface states in the electronic structure of pyrochlore iridates. *Phys. Rev. B* **83**, 205101 (2011).
- Siu, Z. B., Yesilyurt, C., Jalil, M. B. & Tan, S. G. Influence of Fermi arc states and double Weyl node on tunneling in a Dirac semimetal. *Sci. Rep.* **7**, 1–10 (2017).
- Yesilyurt, C., Tan, S. G., Liang, G. & Jalil, M. B. Klein tunneling in Weyl semimetals under the influence of magnetic field. *Sci. Rep.* **6**, 38862 (2016).
- O'Brien, T., Diez, M. & Beenakker, C. Magnetic breakdown and Klein tunneling in a type-II Weyl semimetal. *Phys. Rev. Lett.* **116**, 236401 (2016).
- Yang, S. A., Pan, H. & Zhang, F. Chirality-dependent Hall effect in Weyl semimetals. *Phys. Rev. Lett.* **115**, 156603 (2015).
- Yang, K.-Y., Lu, Y.-M. & Ran, Y. Quantum Hall effects in a Weyl semimetal: possible application in pyrochlore iridates. *Phys. Rev. B* **84**, 075129 (2011).
- Ezawa, M. Spin valleytronics in silicene: quantum spin Hall–quantum anomalous Hall insulators and single-valley semimetals. *Phys. Rev. B* **87**, 155415 (2013).
- Xu, G., Weng, H., Wang, Z., Dai, X. & Fang, Z. Chern semimetal and the quantized anomalous Hall effect in HgCr_2Se_4 . *Phys. Rev. Lett.* **107**, 186806 (2011).
- Cortijo, A., Kharzeev, D., Landsteiner, K. & Vozmediano, M. A. Strain-induced chiral magnetic effect in Weyl semimetals. *Phys. Rev. B* **94**, 241405 (2016).
- Chang, M.-C. & Yang, M.-F. Chiral magnetic effect in a two-band lattice model of Weyl semimetal. *Phys. Rev. B* **91**, 115203 (2015).
- Burkov, A. Topological semimetals. *Nat. Mater.* **15**, 1145–1148 (2016).
- Yesilyurt, C., Siu, Z. B., Tan, S. G., Liang, G. & Jalil, M. B. Conductance modulation in Weyl semimetals with tilted energy dispersion without a band gap. *J. Appl. Phys.* **121**, 244303 (2017).
- Yesilyurt, C. et al. Anomalous tunneling characteristic of Weyl semimetals with tilted energy dispersion. *Appl. Phys. Lett.* **111**, 063101 (2017).
- Yesilyurt, C. et al. Electrically tunable valley polarization in Weyl semimetals with tilted energy dispersion. *Sci. Rep.* **9**, 1–16 (2019).
- Xu, N. et al. Discovery of Weyl semimetal state violating Lorentz invariance in MoTe_2 . arXiv:1604.02116 (2016).
- Xu, S.-Y. et al. Discovery of Lorentz-violating type II Weyl fermions in LaAlGe . *Sci. Adv.* **3**, e1603266 (2017).
- Soluyanov, A. A. et al. Type-II Weyl semimetals. *Nature* **527**, 495–498 (2015).
- Deng, K. et al. Experimental observation of topological Fermi arcs in type-II Weyl semimetal MoTe_2 . *Nat. Phys.* **12**, 1105–1110 (2016).
- Kumar, N. et al. Extremely high magnetoresistance and conductivity in the type-II Weyl semimetals WP_2 and MoP_2 . *Nat. Commun.* **8**, 1–8 (2017).
- Jiang, J. et al. Signature of type-II Weyl semimetal phase in MoTe_2 . *Nat. Commun.* **8**, 13973 (2017).
- Sharma, G., Goswami, P. & Tewari, S. Chiral anomaly and longitudinal magnetotransport in type-II Weyl semimetals. *Phys. Rev. B* **96**, 045112 (2017).
- Rafi-Ul-Islam, S., Siu, Z. B., Sun, C. & Jalil, M. B. Realization of Weyl semimetal phases in topoelectrical circuits. *N. J. Phys.* **22**, 023025 (2020).
- Ezawa, M. Higher-order topological electric circuits and topological corner resonance on the breathing Kagome and pyrochlore lattices. *Phys. Rev. B* **98**, 201402 (2018).
- Luo, K. et al. Topological nodal states in circuit lattice. *Research* **2018**, 6793752 (2018).
- Ezawa, M. Electric circuits for non-Hermitian Chern insulators. *Phys. Rev. B* **100**, 081401 (2019).
- Lu, Y. et al. Probing the Berry curvature and Fermi arcs of a Weyl circuit. *Phys. Rev. B* **99**, 020302 (2019).
- Helbig, T. et al. Band structure engineering and reconstruction in electric circuit networks. *Phys. Rev. B* **99**, 161114 (2019).
- Datta, S. & Das, B. Electronic analog of the electro-optic modulator. *Appl. Phys. Lett.* **56**, 665–667 (1990).
- Datta, S. *Quantum Transport: Atom to Transistor* Ch. 9 (Cambridge University Press, Cambridge, 2005).

Acknowledgements

This work is supported by the MOE Tier-I FRC grant (NUS Grant No. R-263-000-D66-114), MOE Tier-II grant MOE2018-T2-2-117 (NUS Grant No. R-398-000-092-112), and other MOE grants (NUS Grant Nos. C-261-000-207-532, and C-261-000-777-532).

Author contributions

All the authors initiated the primary idea. S.M.R.-U.-I. and Z.B.S. formulated the analytical model, developed the code, analyzed the data, and wrote the manuscript. M.B.A.J. contributed to the discussion and manuscript, and supervised the overall project.

Competing interests

The authors declare no competing interests.

Additional information

Supplementary information is available for this paper at <https://doi.org/10.1038/s42005-020-0336-0>.

Correspondence and requests for materials should be addressed to M.B.A.J.

Reprints and permission information is available at <http://www.nature.com/reprints>

Publisher's note Springer Nature remains neutral with regard to jurisdictional claims in published maps and institutional affiliations.



Open Access This article is licensed under a Creative Commons Attribution 4.0 International License, which permits use, sharing, adaptation, distribution and reproduction in any medium or format, as long as you give appropriate credit to the original author(s) and the source, provide a link to the Creative Commons license, and indicate if changes were made. The images or other third party material in this article are included in the article's Creative Commons license, unless indicated otherwise in a credit line to the material. If material is not included in the article's Creative Commons license and your intended use is not permitted by statutory regulation or exceeds the permitted use, you will need to obtain permission directly from the copyright holder. To view a copy of this license, visit <http://creativecommons.org/licenses/by/4.0/>.

© The Author(s) 2020